Research Article | Open Access

Catalysis, Energy and Environment

Zhang *et al. Catal. Energy Environ.* **2026**, *1*, 10 **DOI:**10.20517/cee.2026.21

Rare-earth-cation effects in $CuO/Ln_2Ce_2O_7$ catalysts for methanol steam reforming

Tingting Zhang[1], Xin Liu[1], Xinran Pang[1], Yiyun Ke[1], Junwei Xu[2,*], Jiamei Ma[1,*], Xiang Wang[1,*]

Keywords:
Methanol steam reforming, defective fluorite, oxygen exchange, Cu-support interactions, low CO selectivity

Citation: Zhang, T.; Liu, X.; Pang, X.; Ke, Y.; Xu, J.; Ma, J.; Wang, X. Rare-earth-cation effects in $CuO/Ln_2Ce_2O_7$ catalysts for methanol steam reforming. *Catal. Energy Environ.* **2026**, *1*, 10. https://dx.doi.org/10.20517/cee.2026.21

Received: 31 Aug 2026 **First Decision:** 12 Oct 2026 **Revised:** 12 Nov 2026 **Accepted:** 13 Nov 2026 **Published:** 26 Nov 2026

Academic Editor: Chai-Siang Piao
Copy Editor: Shu-Yuan Duan
Production Editor: Shu-Yuan Duan

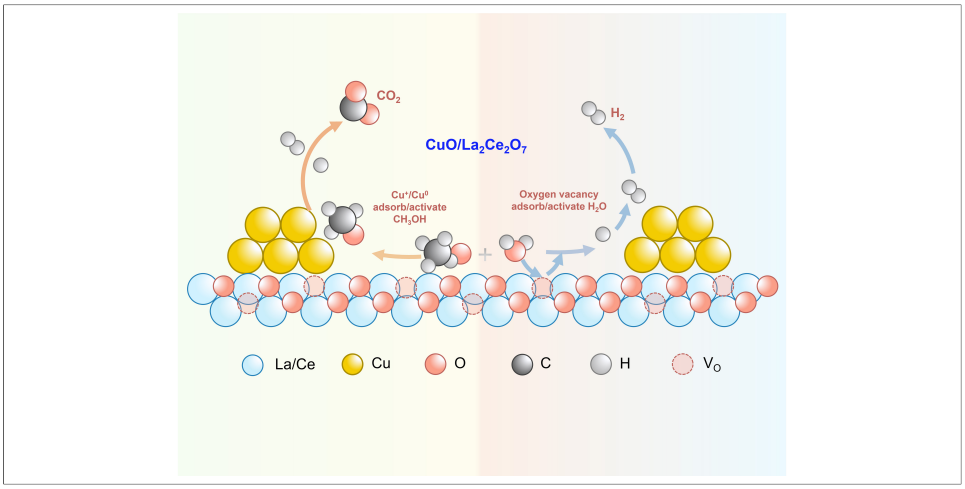

Abstract

Developing efficient Cu-based catalysts with high hydrogen production rates and low CO selectivity is essential for methanol steam reforming (MSR) in on-board hydrogen supply systems. Herein, a series of $CuO/Ln_2Ce_2O_7$ (Ln = La, Nd, Sm, and Y) catalysts supported on defective fluorite-type oxides were prepared and evaluated for MSR. Among the catalysts, $CuO/La_2Ce_2O_7$ exhibited the highest activity, achieving 741 mmol $H_2 \cdot g_{cat} \cdot h^{-1}$ and a relatively low CO selectivity of 1.7% at 360 °C. X-ray diffraction (XRD) and Raman results revealed the highest proportion of surface-adsorbed oxygen species on $CuO/La_2Ce_2O_7$. Furthermore, $^{18}O_2$ isotope-exchange experiments showed that this catalyst had the lowest oxygen-exchange onset temperature (145 °C) and the fastest oxygen-exchange rate. CO_2-TPD further revealed its largest population of weak basic sites. XPS and Cu Auger analysis also highlighted the importance of the $Cu^+ + Cu^0$ amount in determining catalytic activity. *In situ* diffuse reflectance infrared Fourier transform spectroscopy (DRIFTS) detected methoxy and formate species on all four catalysts, consistent with a possible formate-mediated pathway. These findings establish a correlation between rare-earth cation selection, surface oxygen mobility, basic sites, Cu redox properties, and MSR performance,

[1]Key Laboratory of Jiangxi Province for Environment and Energy Catalysis, School of Chemistry and Chemical Engineering, Nanchang University, Nanchang 330031, Jiangxi, China.
[2]Jiangxi Academy of Sciences, Nanchang 330096, Jiangxi, China.

[*]**Correspondence to:** Dr. Jiamei Ma, Jiangxi Academy of Sciences, Nanchang 330096, Jiangxi, China. E-mail: majiamei@ncu.edu.cn; Dr. Junwei Xu, Prof. Xiang Wang, Key Laboratory of Jiangxi Province for Environment and Energy Catalysis, School of Chemistry and Chemical Engineering, Nanchang University, Nanchang 330031, Jiangxi, China. E-mail: xujunwei@email.ncu.edu.cn; xwang23@ncu.edu.cn

providing insights into the design of efficient Cu-based catalysts for MSR.

INTRODUCTION

The growing demand for clean and efficient energy has stimulated the development of hydrogen production technologies. Hydrogen is a promising energy carrier because of its high energy density and zero carbon emissions at the point of use. However, its storage and transportation remain challenging because of safety concerns, high costs, and limited infrastructure[1-3]. Methanol is an attractive liquid hydrogen carrier because it is easy to store and transport and is compatible with existing fuel distribution infrastructure. Methanol steam reforming (MSR) therefore offers a practical route for on-board hydrogen production, particularly for proton exchange membrane fuel cells (PEMFCs)[4,5].

The development of efficient MSR catalysts remains essential for achieving high hydrogen production rates while minimizing CO formation. Ni-based catalysts generally exhibit good reforming activity, but their tendency to produce CO can compromise PEMFC performance[6-10]. Noble-metal catalysts often provide high activity and durability, although their high cost limits large-scale application[11,12]. Cu-based catalysts are attractive because of their relatively low cost and favorable selectivity toward hydrogen-rich products under suitable reaction conditions[13-15]. However, Cu species can undergo sintering during prolonged operation, leading to the loss of accessible active sites and reduced catalytic stability[15-19]. Previous studies have demonstrated that interfacial engineering can improve the performance of Cu-based catalysts. For example, interface-hydroxyl engineering on an inverse ZrO_2/Cu catalyst enabled CO-free hydrogen production with stable operation over 200 h[20]. Jiang *et al.* optimized the Cu^+/Cu^0 ratio through CrO_x modification, reducing the CO selectivity to 0.16%, achieving methanol conversion as high as 93.2%, and inhibiting Cu sintering[21]. These findings highlight the importance of controlling both the Cu active sites and their interactions with the surrounding oxide support.

The physicochemical properties of oxide supports play a crucial role in determining the dispersion, redox behavior, and catalytic performance of supported Cu species. In particular, strong metal-support interactions can stabilize dispersed Cu species and regulate interfacial charge transfer and oxygen exchange[15,19,22]. Our previous studies have shown that Cu^+ and Cu^0 sites contribute differently to reactant activation during MSR. Cu^+ sites favor CH_3OH adsorption and activation, whereas Cu^0 sites contribute to H_2O adsorption and activation. A suitable balance between these two types of sites is therefore important for achieving high catalytic activity. For example, Jiang *et al.* reported enhanced hydrogen production over Cu supported on α-MoC, which was attributed to strong interfacial bonding between Cu and the support[23]. These results suggest that tailoring the support properties and Cu-support interface is a promising strategy for improving MSR performance.

Ce-based oxides are promising supports because their Ce^{3+}/Ce^{4+} redox couple and oxygen-defect structures can facilitate oxygen storage and exchange[24-26]. Introducing rare-earth cations at the A sites of $Ln_2Ce_2O_7$ (Ln = rare-earth element) provides an additional means of tuning the crystal structure, oxygen-defect concentration, and surface basicity. Previous work has shown that changing the A-site cation can alter the structural characteristics of $Ln_2Ce_2O_7$ and influence its catalytic properties[27,28]. In particular, variations in the rare-earth cation can affect the balance between ordered pyrochlore and disordered defective-fluorite structures. These structural changes may influence oxygen mobility and the surface properties relevant to catalytic reactions. However, the effects of different rare-earth cations on the physicochemical properties and MSR performance of CuO/$Ln_2Ce_2O_7$ catalysts have not been systematically clarified. In particular, the relationships among surface oxygen species, oxygen-exchange behavior, surface basicity, Cu redox properties, and catalytic performance remain to be established for this catalyst series.

In this work, a series of CuO/$Ln_2Ce_2O_7$ catalysts (Ln = La, Nd, Sm, and Y) were prepared and evaluated for MSR. To the best of our knowledge, this is the first application of this defective-fluorite $Ln_2Ce_2O_7$ support family in MSR. Building on our previous studies of rare-earth-oxide-supported Cu catalysts and Cu^+/Cu regulation, the present work focuses on how A-site rare-earth-cation selection within the $Ln_2Ce_2O_7$ series influences catalytic activity and stability. A combination of X-ray diffraction (XRD), Raman spectroscopy, X-ray photoelectron spectroscopy (XPS), H_2 temperature-programmed reduction (H_2-TPR), CO_2 temperature-programmed desorption (CO_2-TPD), transmission electron microscopy (TEM), *in situ* diffuse reflectance infrared Fourier transform spectroscopy (DRIFTS), and $^{18}O_2$ isotope-exchange experiments was used to examine the relationships among structural properties, surface oxygen species, oxygen-exchange behavior, surface basicity, Cu dispersion, Cu redox properties, and MSR performance. This comparative study aims to clarify the role of the rare-earth cation in regulating these interconnected properties and to provide guidance for designing Cu-based MSR catalysts with improved hydrogen production performance and low CO selectivity.

EXPERIMENTAL

Catalyst preparation

$Ln_2Ce_2O_7$ defective fluorite-type oxide supports with different A-site rare-earth cations were synthesized by coprecipitation. Stoichiometric amounts of analytical-grade $Ce(NO_3)_4{\cdot}6H_2O$ and $Ln(NO_3)_3{\cdot}xH_2O$ were dissolved in deionized water under continuous stirring to form a clear mixed solution. Aqueous ammonia was added dropwise to adjust the pH to 9, ensuring complete precipitation of the metal cations. The suspension was stirred at room temperature for 2 h at 500 rpm. The precipitate was collected by vacuum filtration and washed repeatedly with deionized water until the total dissolved solids in the filtrate were below 20 ppm. The filter cake was dried at 110 °C for 12 h, ground into a fine powder, and calcined at 600 °C for 4 h at a heating rate of 2 °C·min^{-1} to obtain the $Ln_2Ce_2O_7$ supports.

CuO/$Ln_2Ce_2O_7$ (Ln = La, Nd, Sm, and Y) catalysts were prepared by wet impregnation. In a typical synthesis, 1.86 g of $Ln_2Ce_2O_7$ support and a calculated amount of analytical-grade $Cu(NO_3)_2$ (corresponding to a CuO loading of 7 wt.%) were dispersed in deionized water. The total mass of CuO and $Ln_2Ce_2O_7$ was fixed at 2 g. The suspension was stirred at room temperature and then evaporated to dryness in a water bath at 90 °C. The obtained solid was ground and calcined at 400 °C for 4 h at a heating rate of 2 °C·min^{-1}. After cooling and regrinding, the CuO/$Ln_2Ce_2O_7$ catalysts were obtained. The Cu contents of all the catalysts were validated by ICP-OES [Supplementary Table 1] and agreed with the calculated amounts within experimental error.

Catalyst characterization

The physicochemical properties of the catalysts were examined by XRD, Raman spectroscopy, XPS, ICP-OES, N_2 adsorption-desorption, N_2O titration, TEM, high-resolution transmission electron microscopy (HRTEM), scanning transmission electron microscopy (STEM)-mapping, H_2-TPR, CO_2-TPD, and *in situ* DRIFTS. Detailed instrument models, experimental procedures, reaction conditions, and operating parameters are provided in the Supplementary Materials.

Catalytic performance evaluation

The catalytic performance of the catalysts for the MSR was evaluated in a fixed-bed quartz tubular microreactor (i.d. = 6 mm) at 1 atm. Typically, 100 mg of sample was first reduced *in situ* in a 10 vol% H_2/Ar flow of 30 mL·min^{-1} at 300 °C for 40 min. Then, the reaction feedstock with a CH_3OH/H_2O molar ratio of 1/1.5 at a flow rate of 0.05 mL·min^{-1} was brought into a pre-heated chamber using a micro pump, in which the temperature was controlled at 200 °C to completely evaporate the liquids into steam and then mix with an Ar flow. The weight hourly space velocity (WHSV) of the reaction based on the liquid flow is 27 h^{-1}. After

the reaction, the product gas mixture flow was condensed by a cold-water trap first, and then analyzed online on a GC9310 gas chromatograph equipped with a TDX-01 column and a thermal conductivity detector using a 99.99% Ar flow as the carrier gas to monitor the concentrations of H_2, CO_2, and CO.

The CH_3OH conversion (X_{MeOH}), H_2 production rate (R_{H2}), CO selectivity (S_{CO}), and CO_2 selectivity (S_{CO2}) over catalysts were calculated according to the following equations:

CH_3OH conversion:

$$X_{CH_3OH}(\%) = \frac{F_{out} \times (\Phi_{CO} + \Phi_{CO_2}) \times (32 \times 1 + 18 \times 1.5)}{F_{in} \times \rho \times 22.4 \times 1000} \times 100\% \quad (1)$$

CO_2 selectivity:

$$S_{CO_2}(\%) = \frac{\Phi_{CO_2}}{(\Phi_{CO} + \Phi_{CO_2})} \times 100\% \quad (2)$$

CO selectivity:

$$S_{CO}(\%) = 1 - SCO_2(\%) \quad (3)$$

$$R_{H_2}\left(\text{mmol} \cdot \ {g_{cat}}^{-1} \cdot \ h^{-1}\right) = \text{conversion } CH_3OH \times \frac{\text{WHSV}}{1 \times M_{CH_3OH} + 1.5 \times M_{H_2O}} \times 3 \times 1000 \quad (4)$$

In Equation 1, Fout is the flow rate of reforming gas under standard conditions (mL·min^{-1}); Fin represents the inlet flow rate (mL·min^{-1}) of the CH_3OH and H_2O solution mixture, whose density (ρ = 0.9, g·mL^{-1}) was measured with a density meter; in Equations 2 and 3, Φ_{CO} and Φ_{CO_2} represent the amount of CO and CO_2 obtained by the corresponding response factors and integrated peak areas. In Equation (4), the numbers 3 and 1,000 in the H_2 production rate calculation are the standard molar ratio of the equation: $CH_3OH + H_2O \rightarrow 3H_2 + CO_2$, in which 3 moles of hydrogen will be produced with 1 mole of methanol conversion and the unit conversion (mole to millimole), respectively.

$$\text{WHSV} = (0.05 \text{ mL·min}^{-1} \times 60 \text{ min·h}^{-1} \times 0.9 \text{ g·mL}^{-1}) / 0.1 \text{ g} = 27 \text{ h}^{-1}.$$

Here, 0.05 mL·min^{-1} is the volumetric flow rate of the liquid feed, and 0.9 g·mL^{-1} is the density of the liquid methanol-water mixture.

The Arrhenius plots are obtained for all the catalysts with CH_3OH conversions below ~ 10% to obtain the differential reaction rates (R_w and R_S) in the kinetic regime. By adjusting the catalyst amount, the methanol conversions were collected over the temperature range of 180-210 °C. The turnover frequencies (TOFs) were calculated based on the exposed surface Cu active sites using metallic Cu dispersion determined by N_2O titration of the reduced catalysts. The equations to calculate R_w and TOF are listed here:

$$R_W = \frac{RF \times \rho \times \text{mol}^{-1} \times X_{CH_3OH}}{m_{cat} \times \left(32 \times \frac{1}{2.5} + 18 \times \frac{1.5}{2.5}\right)}$$

R_w is the CH_3OH conversion rate normalized by catalyst mass. RF is the reaction feed flow rate (mL·min^{-1}), ρ is the density of the reaction feed (g·mL^{-1}) measured with a density analyzer, X_{CH_3OH} is the CH_3OH conversion (%), mol% is the molar fraction of CH_3OH in the reaction feed, m_{cat} is the mass of catalyst (0.05 g), and S_{cat} is the specific surface area of catalyst (m^2/g).

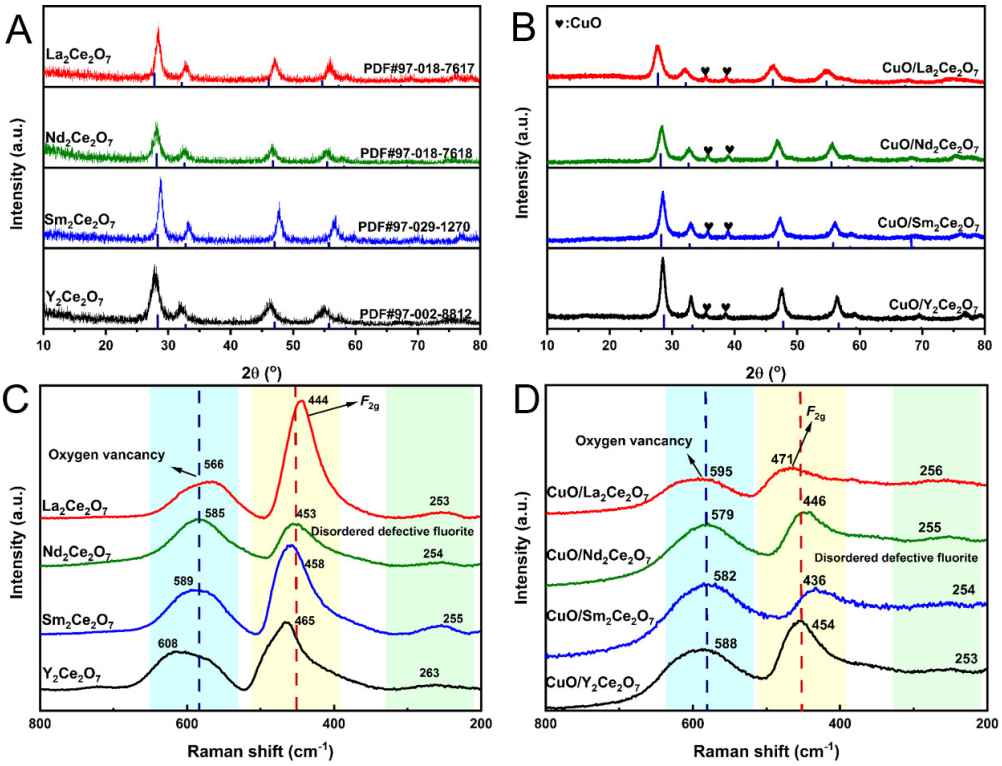

Figure 1. (A) XRD patterns of the supports; (B) XRD patterns of the fresh catalysts; (C) Raman spectra of the supports; (D) Raman spectra of the fresh catalysts. XRD: X-ray diffraction.

$$\mathrm{TOF} = \frac{R_w \times \mathrm{M}_{Cu}}{X_{Cu} \times D_{Cu}}$$

M_{Cu} (63.5 g/mol) is the atomic molar mass of Cu, X_{Cu} is the metal content (g_{Cu}/g_{cat}), D_{Cu} is the Cu dispersion. The total Cu content used for TOF calculation was 7 wt.% as CuO, as determined by ICP-OES [Supplementary Table 1]. All surface Cu atoms were assumed to be active sites for the MSR reaction.

RESULTS AND DISCUSSION

Structural and textural properties of the catalysts

XRD was used to examine the crystalline phases and structural properties of the prepared catalysts. As shown in Figure 1A and B, the diffraction patterns were consistent with the standard powder diffraction file (PDF) reference patterns of $Ln_2Ce_2O_7$ (Ln = La, Nd, Sm, and Y), confirming the formation of the defective fluorite structure. After CuO loading, all catalysts retained the crystal structure of their respective supports. Weak characteristic CuO diffraction peaks were observed for all four catalysts, suggesting slight aggregation of CuO species. The XRD patterns of the reduced and spent catalysts are presented in Supplementary Figure 1A and B. The defective fluorite framework was retained after reduction and MSR, while CuO was reduced to metallic Cu under reducing conditions. These results indicate that the support framework exhibits good structural stability under the investigated conditions.

Raman spectra provided further insight into the structural features of the supports and catalysts. As shown in Figure 1C, the band at approximately 460 cm^{-1} was assigned to the F_{2g} vibrational mode of the defective fluorite framework[29,30]. Additional bands at approximately 256 and 580 cm^{-1} were associated with oxygen-anion disorder and surface oxygen vacancies, respectively, arising from the disordered arrangement of A^{3+} and Ce^{4+} cations[31,32]. No sharp peak splitting characteristic of an ordered structure was observed, supporting the assignment of a defective fluorite structure. After CuO impregnation, these characteristic Raman features

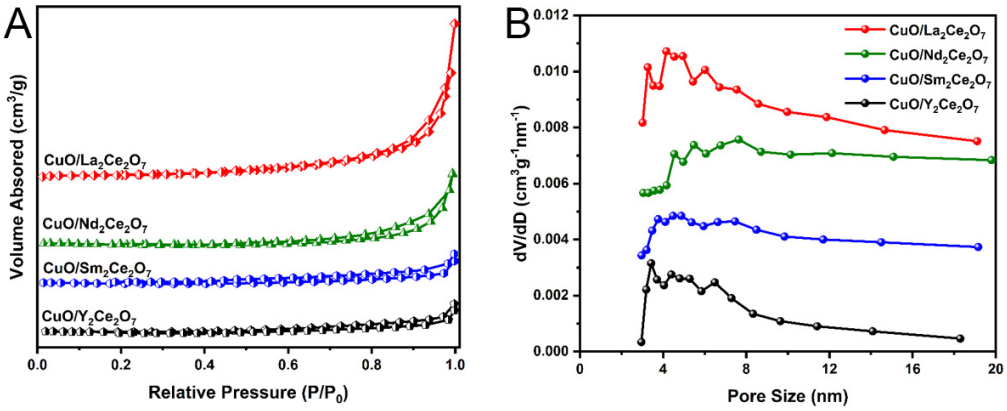

Figure 2. N_2 sorption measurements of the fresh catalysts: (A) isotherms and (B) pore size distribution profiles.

remained unchanged [Figure 1D], indicating that CuO loading did not significantly alter the support structure. As shown in Supplementary Figure 2A and B, broad bands at approximately 460 and 580 cm^{-1} were also observed for all catalysts, while sharp peak splitting associated with a well-ordered structure was absent. These observations further support the preservation of the defective fluorite framework under reducing and MSR conditions.

The textural properties of the catalysts were investigated by N_2 adsorption-desorption measurements. As shown in Figure 2A, all four catalysts exhibited type IV adsorption isotherms with H3-type hysteresis loops. The corresponding pore size distributions [Figure 2B] indicated that the catalysts were predominantly mesoporous, with mesopores likely arising from particle aggregation. As summarized in Supplementary Table 1, the specific surface areas of the fresh catalysts were slightly lower than those of the corresponding supports. This decrease may be attributed to the additional calcination step or partial blockage of the pore channels by CuO species.

HRTEM and STEM elemental mapping were used to examine the microstructure and elemental distribution of the catalysts. As shown in Figure 3A-D, lattice spacings of 0.327 and 0.312 nm were observed in the HRTEM images. These spacings were assigned to the (222) plane of $La_2Ce_2O_7$ and the (111) planes of $Nd_2Ce_2O_7$, $Sm_2Ce_2O_7$, and $Y_2Ce_2O_7$, respectively, in agreement with the XRD results. STEM elemental mapping [Figure 3E-H] revealed a relatively homogeneous distribution of the constituent elements throughout the catalysts. Cu-containing species were also distributed across the support surfaces, although some local particle agglomeration was observed.

MSR performance and kinetic analysis

The catalytic performance of the catalysts for MSR was evaluated under atmospheric pressure. Before the reaction, each catalyst was reduced in a 10 vol% H_2/Ar flow at 300 °C for 40 min. To determine the optimal CuO loading, a series of CuO/$La_2Ce_2O_7$ catalysts with nominal CuO loadings of 1, 3, 5, 7, 9, 11, and 13 wt.% were prepared and evaluated. As shown in Supplementary Figure 3A, the characteristic CuO diffraction peaks became more pronounced with increasing CuO loading, indicating an increase in the amount of crystalline CuO. The H_2 production rate increased with Cu loading from 1 to 7 wt.% and then decreased at higher loadings [Supplementary Figure 3B]. The maximum H_2 production rate was approximately 741 mmol $H_2 \cdot g_{cat} \cdot h^{-1}$ at a Cu loading of 7 wt.%, identifying this loading as optimal within the investigated range. Accordingly, the 7 wt.% CuO/$La_2Ce_2O_7$ catalyst was selected for further comparison with the other catalysts.

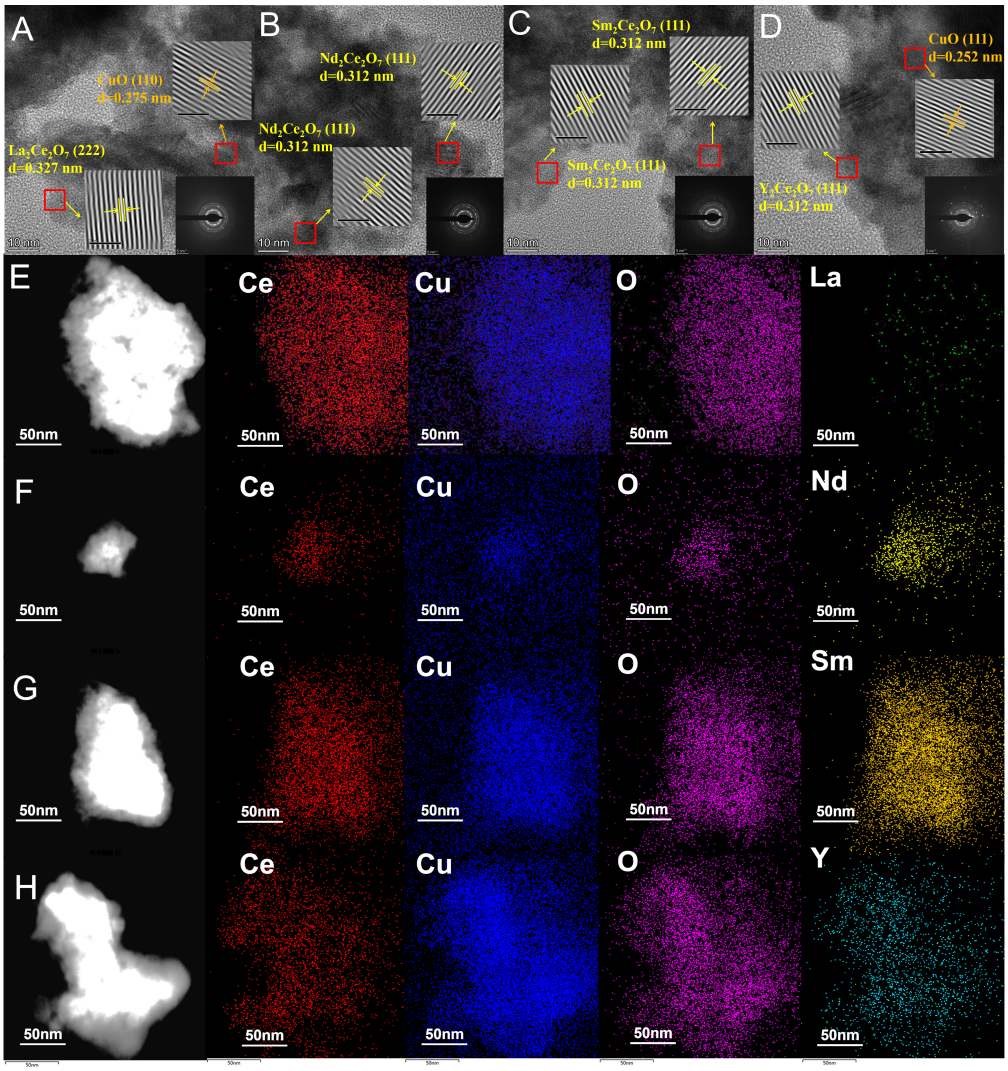

Figure 3. HRTEM images of all the catalysts: (A) $CuO/La_2Ce_2O_7$; (B) $CuO/Nd_2Ce_2O_7$; (C) $CuO/Sm_2Ce_2O_7$; (D) $CuO/Y_2Ce_2O_7$; STEM-mapping results of all the catalysts: (E) $CuO/La_2Ce_2O_7$; (F) $CuO/Nd_2Ce_2O_7$; (G) $CuO/Sm_2Ce_2O_7$; (H) $CuO/Y_2Ce_2O_7$. HRTEM: High-resolution transmission electron microscopy; STEM: scanning transmission electron microscopy。

As shown in Figure 4A, the catalytic activity increased with reaction temperature for all four catalysts. Among them, $CuO/La_2Ce_2O_7$ exhibited the highest activity, achieving 54% CH_3OH conversion at 360 °C, whereas $CuO/Sm_2Ce_2O_7$ showed the lowest conversion. $CuO/La_2Ce_2O_7$ also delivered the highest H_2 production rate, reaching 741 mmol $H_2 \cdot g_{cat} \cdot h^{-1}$ [Figure 4B]. In addition, $CuO/La_2Ce_2O_7$ and $CuO/Y_2Ce_2O_7$ exhibited high CO_2 selectivity and relatively low CO selectivity [Figure 4C].

The stability of the four catalysts was further evaluated by monitoring their H_2 production rates at 180 °C following pretreatment in a 10 vol% H_2/Ar flow at 300 °C for 40 min. As shown in Supplementary Figure 4A-D, $CuO/La_2Ce_2O_7$ and $CuO/Y_2Ce_2O_7$ maintained measurable H_2 production over 50 h, although their H_2 production rates decreased by approximately 44% and 48%, respectively. In contrast, the H_2 production rate of $CuO/Nd_2Ce_2O_7$ decreased from approximately 195 to 77 mmol $H_2 \cdot g_{cat} \cdot h^{-1}$ within 30 h. $CuO/Sm_2Ce_2O_7$ exhibited a more rapid decline, with its H_2 production rate decreasing from approximately 150 to 60 mmol $H_2 \cdot g_{cat} \cdot h^{-1}$ within 10 h. These results reveal differences in the sustained catalytic performance of the four catalysts, with $CuO/La_2Ce_2O_7$ and $CuO/Y_2Ce_2O_7$ maintaining H_2 production for longer periods under the tested conditions. The MSR performance of the $CuO/La_2Ce_2O_7$ catalyst in this work is also compared in Supplementary Figure 5 with those typical catalysts reported previously by other researchers.

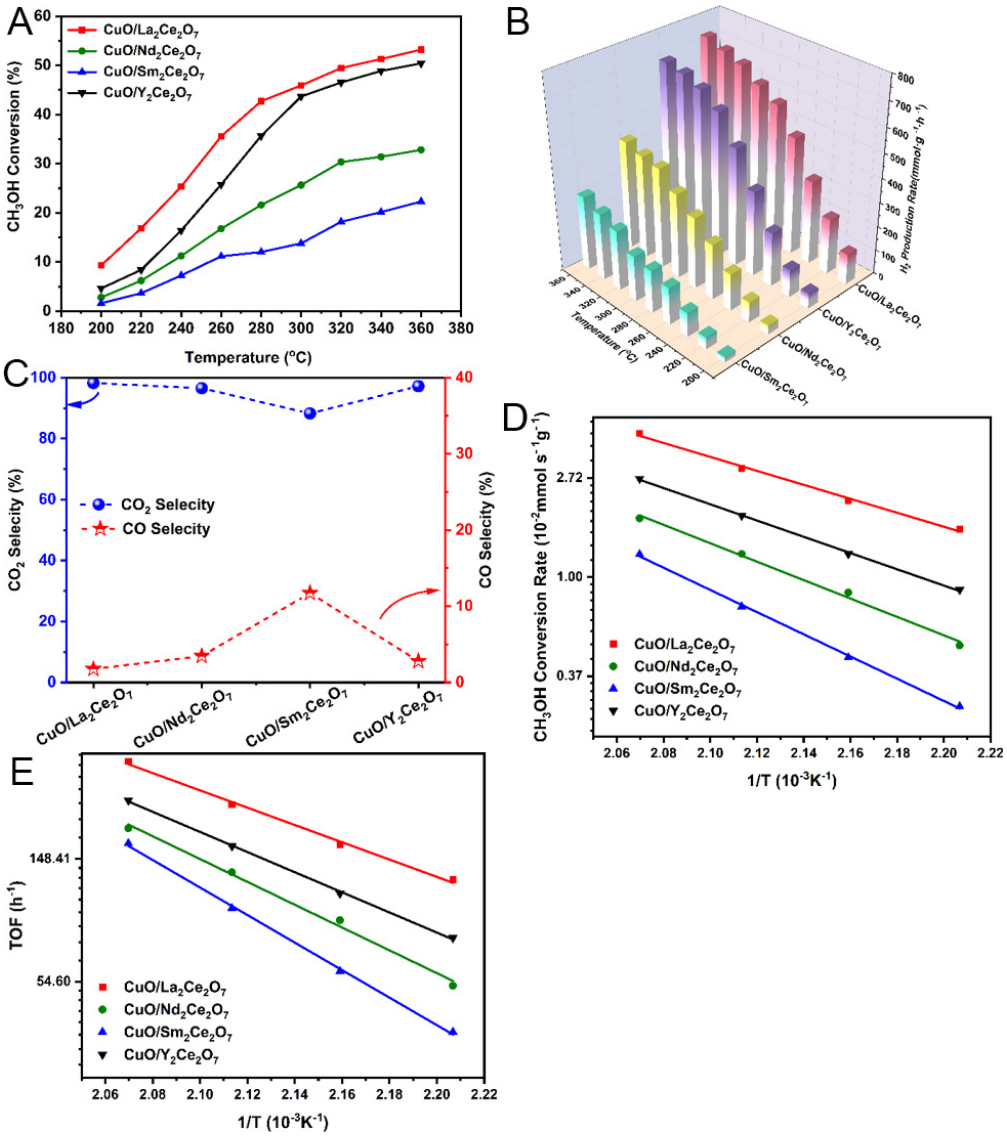

Figure 4. MSR reaction performance of $CuO/Ln_2Ce_2O_7$ (Ln = La, Nd, Sm, and Y) catalysts. (A) CH_3OH conversion; (B) H_2 production rate; (C) CO_2 and CO selectivities at 360 °C; (D) R_w-based Arrhenius plots; (E) TOF-based Arrhenius plots. MSR: Methanol steam reforming; TOF: turnover frequency.

To compare the intrinsic catalytic properties of the four catalysts, kinetic measurements were conducted under differential reaction conditions. CH_3OH conversion was maintained below 10% by adjusting the catalyst amount and reactant flow rate. Although these conditions were intended to minimize mass- and heat-transfer effects, internal and external diffusion limitations could not be completely ruled out. The kinetic measurements of R_w and TOF were performed over the temperature range of 180-210 °C for Arrhenius fitting. For a direct comparison of intrinsic activity, the specific R_w and TOF values obtained at 210 °C are presented in Table 1. The Arrhenius plots based on R_w and TOF are presented in Figure 4D and E, respectively. As summarized in Table 1 and Supplementary Table 2, the R_w values followed the order $CuO/La_2Ce_2O_7$ (4.3×10^{-2} mmol $s^{-1} \cdot g_{cat}^{-1}$) > $CuO/Y_2Ce_2O_7$ (2.7×10^{-2} mmol $s^{-1} \cdot g_{cat}^{-1}$) > $CuO/Nd_2Ce_2O_7$ (1.8×10^{-2} mmol $s^{-1} \cdot g_{cat}^{-1}$) > $CuO/Sm_2Ce_2O_7$ (1.3×10^{-2} mmol $s^{-1} \cdot g_{cat}^{-1}$). The TOF values exhibited the same trend, reaching 329, 239, 191, and 168 h^{-1}, respectively. These results demonstrate that $CuO/La_2Ce_2O_7$ exhibited the highest mass-normalized reaction rate and the highest turnover frequency among the four catalysts.

Table 1. Catalytic kinetics and Cu dispersion of the prepared catalysts

Catalysts	R_w (10^{-2} mmol $\cdot s^{-1} \cdot g^{-1}$)[a]	E_a (kJ $\cdot mol^{-1}$)[b]	TOF (h^{-1})[c]	N_2O titration results[d]		
				Cu active surface area ($m^2 \cdot g_{Cu}^{-1}$)	Cu grain size (nm)	D_{Cu} (%)
$CuO/La_2Ce_2O_7$	4.3	59	329	295.0	2.4	43.6
$CuO/Nd_2Ce_2O_7$	1.8	77	191	216.1	3.3	31.9
$CuO/Sm_2Ce_2O_7$	1.3	93	168	170.1	4.1	25.1
$CuO/Y_2Ce_2O_7$	2.7	68	239	252.9	2.8	37.4

a: The CH_3OH conversion rates at 210 °C were normalized by catalyst mass. (CH_3OH conversion was below 10%, and the catalyst mass was 50 mg (see the Supplementary Materials for experimental details); b: Calculated by Arrhenius equations; c: TOF at 210 °C, calculated based on the CuO content determined by ICP-OES (7 wt.% as CuO, Supplementary Table 1); d: Measured by N_2O titration. TOF: Turnover frequency; ICP-OES:

The E_a derived from the Arrhenius plots were 59, 68, 77, and 93 kJ mol^{-1} for $CuO/La_2Ce_2O_7$, $CuO/Y_2Ce_2O_7$, $CuO/Nd_2Ce_2O_7$, and $CuO/Sm_2Ce_2O_7$, respectively. The lower apparent activation energy of $CuO/La_2Ce_2O_7$ was consistent with its higher reaction rate and TOF, whereas $CuO/Sm_2Ce_2O_7$ exhibited the highest apparent activation energy and the lowest catalytic activity. This trend suggests that the rare-earth cation influences the kinetic behavior of the catalysts.

The N_2O titration results in Table 1 further revealed differences in the accessible Cu surface area, Cu grain size, and Cu dispersion among the catalysts. $CuO/La_2Ce_2O_7$ exhibited the largest Cu active surface area (295.0 $m^2 \cdot g_{Cu}^{-1}$), the smallest Cu grain size (2.4 nm), and the highest Cu dispersion (43.6%). In contrast, $CuO/Sm_2Ce_2O_7$ showed the smallest Cu active surface area (170.1 $m^2 \cdot g_{Cu}^{-1}$), the largest Cu grain size (4.1 nm), and the lowest Cu dispersion (25.1%). $CuO/Nd_2Ce_2O_7$ and $CuO/Y_2Ce_2O_7$ exhibited intermediate values. The Cu dispersion followed the order $CuO/La_2Ce_2O_7$ (43.6%) > $CuO/Y_2Ce_2O_7$ (37.4%) > $CuO/Nd_2Ce_2O_7$ (31.9%) > $CuO/Sm_2Ce_2O_7$ (25.1%), consistent with the trends in R_w and TOF. The correlation between Cu dispersion and catalytic activity suggests that the greater accessibility of Cu surface sites contributes to the superior performance of $CuO/La_2Ce_2O_7$. However, the differences in apparent activation energy also indicate that variations in the intrinsic reactivity of the accessible sites may contribute to the observed activity differences. Overall, these results establish a clear relationship between Cu dispersion, apparent kinetic parameters, and MSR performance across the catalyst series.

Surface chemical states and oxygen-exchange behavior

XPS was used to investigate the surface chemical states of the catalysts. The Ce 3d spectra [Figure 5A] were deconvoluted into ten peaks (v_0-v‴ and u_0-u‴) following a previously reported procedure. The v and u series correspond to the Ce $3d_{5/2}$ and $3d_{3/2}$ components, respectively. The v′ and u′ peaks were assigned to Ce^{3+}, whereas the remaining peaks were attributed to Ce^{4+}[33]. The surface Ce^{3+} fraction followed the order $CuO/La_2Ce_2O_7$ > $CuO/Y_2Ce_2O_7$ > $CuO/Nd_2Ce_2O_7$ > $CuO/Sm_2Ce_2O_7$. The corresponding $Ce^{3+}/(Ce^{3+} + Ce^{4+})$ ratios are summarized in Table 2 and provide further insight into the surface defect chemistry of the catalysts.

The O 1s spectra were further analyzed to investigate the distribution of surface oxygen species and its relationship with catalytic performance [Figure 5B]. Peak fitting allowed the categorization of the O1s spectra into 3 types of oxygen species. The peak around 529.0 eV is attributable to surface lattice O^{2-}, the peak around 531.5 eV corresponds mainly to -OH groups, and the peak near 533.0 eV is assignable to active superoxide O_2^- anions[34]. To quantitatively evaluate the evolution of these oxygen species, it is essential to distinguish their chemical notations. The lattice oxygen is denoted as O^{2-} (where each oxygen atom has a valence of -2), whereas the surface-adsorbed superoxide is denoted as O_2^- (where two oxygen atoms share

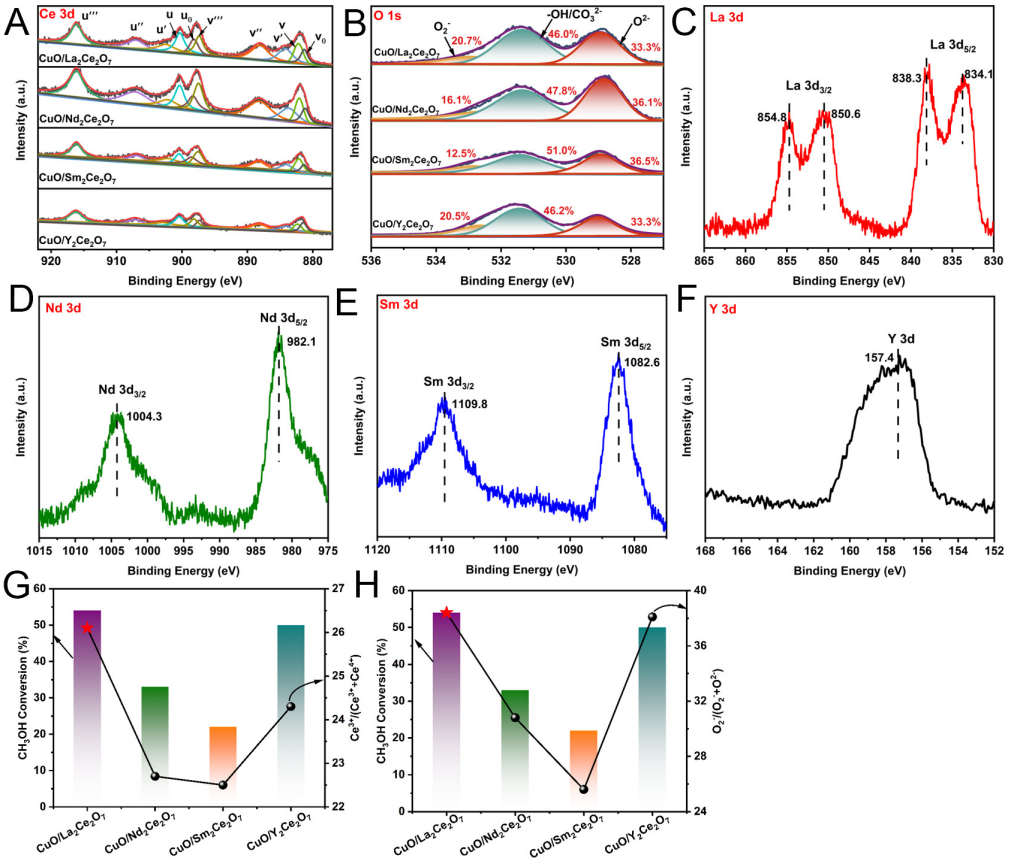

Figure 5. XPS spectra of reduced catalysts: (A) Ce 3d; (B) O 1s. In (A), the black lines represent experimental data, colored lines represent fitted peaks, and the red line represents the cumulative fit. In (B), the black lines represent experimental data, colored lines represent fitted peaks, and the purple line represents the cumulative fit. (C) La 3d; (D) Nd 3d; (E) Sm 3d; (F) Y 3d. (G) Relationship between CH_3OH conversion and $Ce^{3+}/(Ce^{3+}+Ce^{4+})$; (H) Relationship between CH_3OH conversion and $O_2^-/(O_2^-+O^{2-})$. XPS: X-ray photoelectron spectroscopy.

Table 2. Quantified XPS Cu 2p, O 1s, and Ce 3d results of the catalysts

Catalyst	Fraction of low-valence Cu (Cu^0+Cu^+)/($Cu^0+Cu^++Cu^{2+}$) (%) (reduced/spent)[a]	Cu^+/ Cu ratio(reduced/spent)[b]	O1s B.E (eV) / relative amount[c]				Ce 3d B.E (eV) / relative amount[d]
			O_2^- (adsorbed oxygen)	-OH/CO_3^{2-}	O^{2-} (lattice oxygen)	O_2^-/(O_2^-+O^{2-}) (%)	$Ce^{3+}/(Ce^{3+}+Ce^{4+})$ (%)
$CuO/La_2Ce_2O_7$	77.8/74.7	1.02/1.00	532.9/20.7	531.4/46.0	528.9/33.3	38.4	26.1
$CuO/Nd_2Ce_2O_7$	63.5/59.2	0.79/0.72	532.7/16.1	531.4/47.8	528.8/36.1	30.8	22.7
$CuO/Sm_2Ce_2O_7$	52.4/48.8	0.67/0.46	532.9/12.5	531.4/51.0	528.9/36.5	25.5	22.5
$CuO/Y_2Ce_2O_7$	71.7/65.2	0.87/0.82	532.6/20.5	531.4/46.2	529.0/33.3	38.1	24.3

a: Cu 2p XPS results of the reduced and spent catalysts. The total fraction of low-valence Cu is calculated as (Cu^0+Cu^+)/ ($Cu^0+Cu^++Cu^{2+}$) collected from XPS Cu $2p_{2/3}$; b: Auger results of the reduced and spent catalysts. The ratio represents the relative proportion of Cu^+ to Cu^0 species collected from Cu LMM; c: O 1s XPS results of the reduced catalysts; d: Ce 3d XPS results of the reduced catalysts. XPS: X-ray photoelectron spectroscopy.

one electron, averaging a valence of $-\frac{1}{2}$ per oxygen atom). The relative contributions of these oxygen species are summarized in Table 2. $CuO/La_2Ce_2O_7$ exhibited the highest proportion of O_2^- (20.7%), closely followed by $CuO/Y_2Ce_2O_7$ (20.5%). The corresponding values for $CuO/Nd_2Ce_2O_7$ and $CuO/Sm_2Ce_2O_7$ were 16.1% and 12.5%, respectively. This trend was consistent with the catalytic activity order, suggesting that surface-adsorbed oxygen species may contribute to the differences in MSR performance[35].

The La 3d, Nd 3d, Sm 3d, and Y 3d spectra [Figure 5C-F] were also examined to determine the oxidation states of the rare-earth elements. The observed binding energies were consistent with the predominantly trivalent states of La, Nd, Sm, and Y in the respective catalysts. To further examine the relationships between surface chemical properties and catalytic performance, the Ce^{3+}/ (Ce^{3+} + Ce^{4+}) and O_2^-/ (O_2^- + O^{2-}) ratios were plotted against CH_3OH conversion in Figure 5G and H, respectively. $CuO/La_2Ce_2O_7$ and $CuO/Y_2Ce_2O_7$ exhibited relatively high Ce^{3+} fractions and O_2^-/ (O_2^- + O^{2-}) ratios, consistent with their higher catalytic activities. These correlations suggest that the surface redox properties and adsorbed oxygen species are associated with MSR performance. The differences in Ce^{3+} content may also reflect variations in the defect chemistry of the supports, which could influence oxygen-related surface processes during MSR.

The XPS O 1s results suggested a potential relationship between surface oxygen species and catalytic performance. Therefore, $^{18}O_2$ isotope-exchange experiments were conducted to compare the oxygen-exchange behavior of the $CuO/Ln_2Ce_2O_7$ (Ln = La, Nd, Sm, and Y) catalysts [Figure 6A-D]. Oxygen isotope exchange on metal oxides can proceed through two pathways. In the R1 pathway, known as simple hetero-exchange, gaseous $^{18}O_2$ exchanges with lattice ^{16}O to form $^{16}O^{18}O$. In the R2 pathway, known as multiple hetero-exchange, gaseous $^{18}O_2$ reacts with lattice oxygen to form $^{16}O_2$, while ^{18}O is incorporated into the catalyst lattice[36,37]. The formation of $^{16}O^{18}O$ and $^{16}O_2$ was monitored by mass spectrometry to evaluate the oxygen-exchange behavior of the catalysts.

As the temperature increased, the mass signals associated with $^{16}O^{18}O$ and $^{16}O_2$ increased, indicating enhanced oxygen isotope exchange. Among the four catalysts, $CuO/La_2Ce_2O_7$ exhibited the lowest oxygen-exchange onset temperature, approximately 145 °C, and the lowest temperature for the maximum $^{16}O_2$ signal, approximately 271 °C [Figure 6A]. The corresponding onset and peak temperatures were approximately 175 and 312 °C for $CuO/Nd_2Ce_2O_7$, 193 and 343 °C for $CuO/Sm_2Ce_2O_7$, and 164 and 289 °C for $CuO/Y_2Ce_2O_7$, respectively [Figure 6B-D]. These results indicate that oxygen isotope exchange occurred more readily on $CuO/La_2Ce_2O_7$ than on the other catalysts. $CuO/Y_2Ce_2O_7$ exhibited the second-lowest onset and peak temperatures, whereas $CuO/Sm_2Ce_2O_7$ showed the highest temperatures for both features.

The oxygen-exchange trends are consistent with the relatively high catalytic activities of $CuO/La_2Ce_2O_7$ and $CuO/Y_2Ce_2O_7$. The lower onset and peak temperatures suggest that oxygen exchange is facilitated on these catalysts, potentially reflecting differences in oxygen mobility and surface redox properties. Such properties may contribute to the activation of oxygen-containing reactants and the overall MSR performance. However, the isotope-exchange results alone do not establish a direct causal relationship between oxygen mobility and catalytic activity.

Copper speciation and redox stability under MSR conditions

The Cu oxidation state is an important factor influencing MSR performance[38]. Therefore, Cu 2p XPS and Cu LMM Auger spectra were collected to characterize the copper species in the reduced and spent catalysts. The Cu 2p spectra of the reduced catalysts [Figure 7A] revealed the coexistence of Cu^{2+} and low-valence copper species (Cu^+ and Cu^0) on all four catalysts[39]. However, Cu^+ and Cu^0 cannot be reliably distinguished by Cu 2p XPS alone. Cu LMM Auger spectra were therefore analyzed to distinguish these species and determine the Cu^+/Cu^0 ratios [Figure 7B-E].

As summarized in Figure 7F and Table 2, the Cu^+/Cu^0 ratio of the reduced catalysts followed the order $CuO/La_2Ce_2O_7$ (1.02) > $CuO/Y_2Ce_2O_7$ (0.87) > $CuO/Nd_2Ce_2O_7$ (0.79) > $CuO/Sm_2Ce_2O_7$ (0.67). $CuO/La_2Ce_2O_7$ exhibited the highest CH_3OH conversion and the highest Cu^+/Cu^0 ratio among the four catalysts. This result is consistent with previous studies showing that the balance between Cu^+ and Cu^0 sites can influence MSR activity[40]. Nevertheless, the activity differences cannot be attributed solely to the Cu^+/Cu^0 ratio, as the

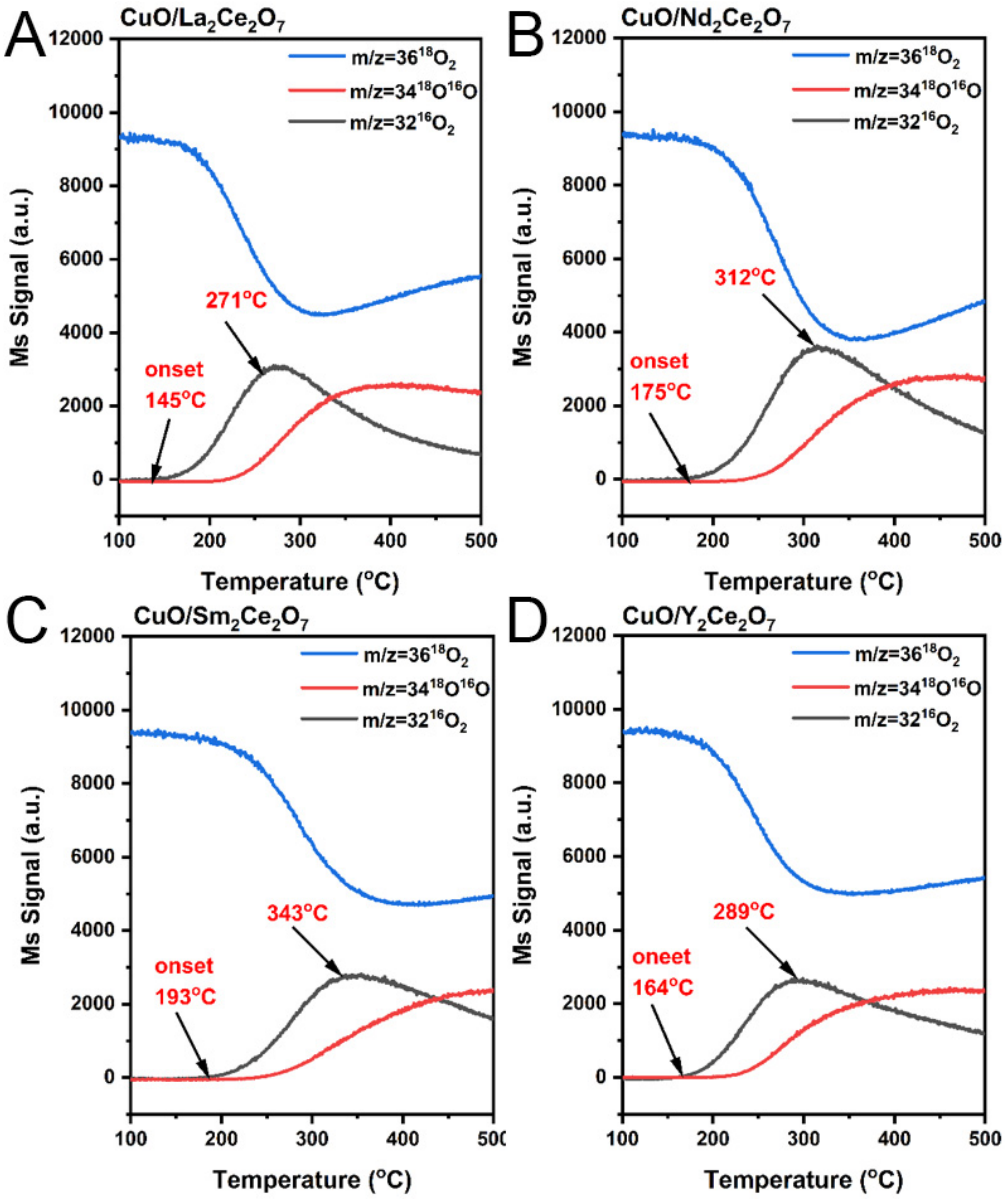

Figure 6. $^{18}O_2$ isotope-exchange experiments over the catalysts, (A) $CuO/La_2Ce_2O_7$; (B) $CuO/Nd_2Ce_2O_7$; (C) $CuO/Sm_2Ce_2O_7$, and (D) $CuO/Y_2Ce_2O_7$.

catalysts also differ in Cu dispersion, surface oxygen species, and other physicochemical properties.

The Cu species were further examined after MSR to evaluate changes in their oxidation states under reaction conditions. The Cu 2p spectra of the spent catalysts are presented in Figure 8A, while the corresponding Cu LMM Auger spectra are shown in Figure 8B-E. As summarized in Figure 8F and Table 2, the Cu^+/Cu^0 ratio decreased after reaction for $CuO/Nd_2Ce_2O_7$, $CuO/Sm_2Ce_2O_7$, and $CuO/Y_2Ce_2O_7$, from 0.79 to 0.72, from 0.67 to 0.46, and from 0.87 to 0.82, respectively. In contrast, the ratio for $CuO/La_2Ce_2O_7$ remained nearly unchanged, decreasing only slightly from 1.02 to 1.00. The particularly pronounced decrease for $CuO/Sm_2Ce_2O_7$ suggests a greater change in its surface copper speciation during MSR, whereas $CuO/La_2Ce_2O_7$ largely retained its initial Cu^+/Cu^0 balance. These findings indicate that the evolution of copper oxidation states depends on the rare-earth cation in the support. The relatively stable Cu^+/Cu^0 ratio of $CuO/La_2Ce_2O_7$, together with its high catalytic activity, suggests that maintaining an appropriate balance of Cu species may contribute to sustained MSR performance.

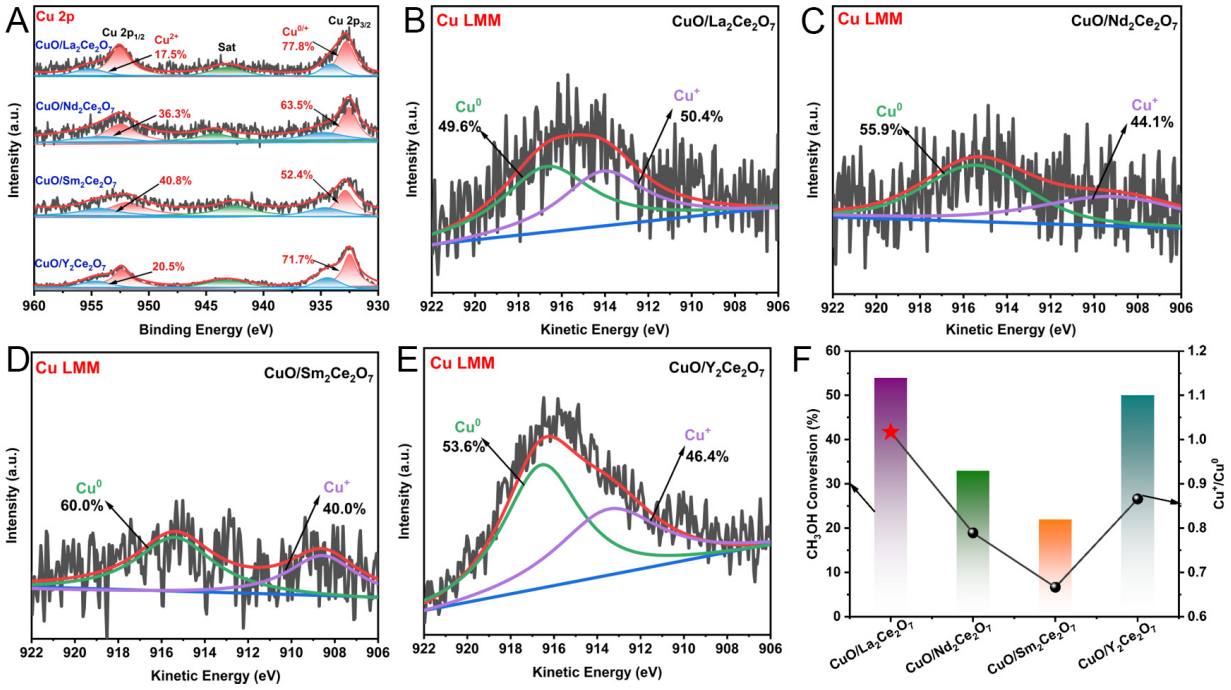

Figure 7. (A) XPS Cu 2p spectra of the reduced catalysts; Auger spectra of the reduced catalysts: (B) $CuO/La_2Ce_2O_7$; (C) $CuO/Nd_2Ce_2O_7$; (D) $CuO/Sm_2Ce_2O_7$; (E) $CuO/Y_2Ce_2O_7$; [In (A-E), the black lines represent experimental data, the colored lines represent fitted peaks, the red lines represent the cumulative fit, and the blue lines represent the background]; (F) CH_3OH conversion at 360 °C versus Cu^+/Cu^0 ratio. XPS: X-ray photoelectron spectroscopy.

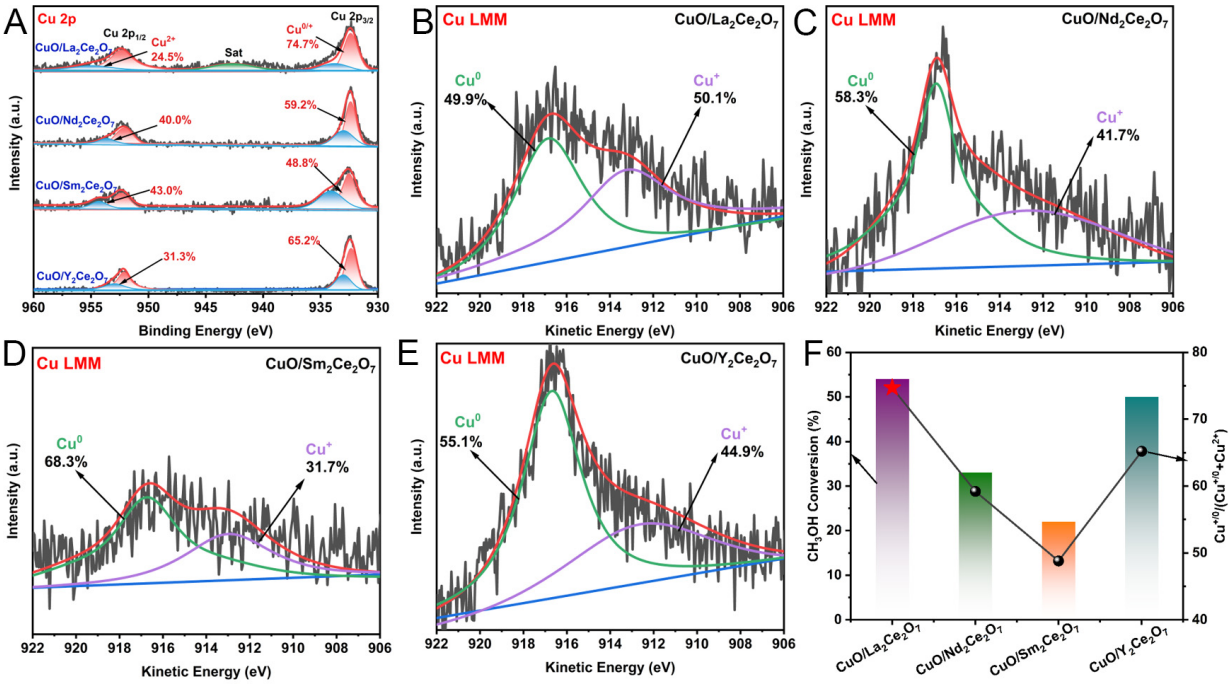

Figure 8. (A) XPS Cu 2p spectra of spent catalysts; Auger spectra of spent catalysts: (B) $CuO/La_2Ce_2O_7$; (C) $CuO/Nd_2Ce_2O_7$; (D) $CuO/Sm_2Ce_2O_7$; (E) $CuO/Y_2Ce_2O_7$. [In (A-E), the black lines represent experimental data, the colored lines represent fitted peaks, the red lines represent the cumulative fit, and the blue lines represent the background]; (F) methanol conversion at 360 °C versus $Cu^{+/0}/(Cu^{+/0}+Cu^{2+})$ ratio of spent catalysts. XPS: X-ray photoelectron spectroscopy.

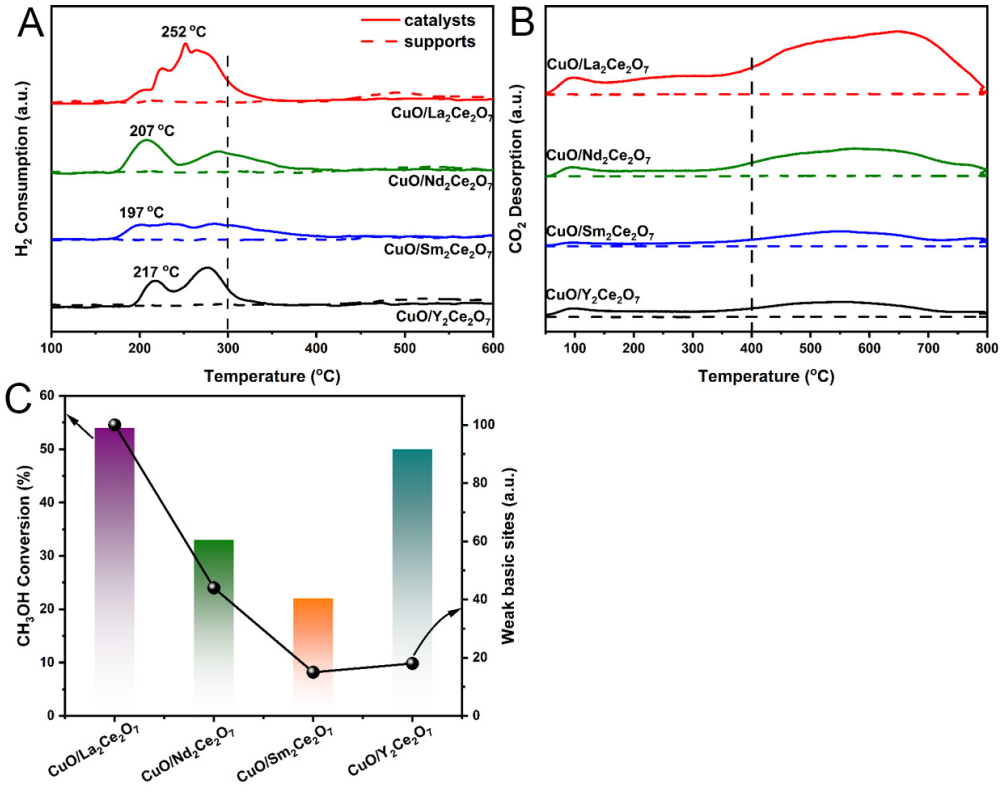

Figure 9. (A) H_2-TPR profiles of the catalysts; (B) CO_2-TPD patterns of the catalysts; (C) The relationship between CH_3OH conversion and the number of weak basic sites. TPR: Temperature-programmed reduction; TPD: temperature-programmed desorption.

Reducibility and surface basicity

H_2-TPR was used to investigate the reduction behavior of the copper species. As shown in Figure 9A, the bare supports exhibited reduction signals at higher temperatures. For the supported catalysts, the main reduction peaks below 300 °C were primarily attributed to the reduction of CuO species. The peak maxima were observed at 252, 207, 197, and 217 °C for $CuO/La_2Ce_2O_7$, $CuO/Nd_2Ce_2O_7$, $CuO/Sm_2Ce_2O_7$, and $CuO/Y_2Ce_2O_7$, respectively. Notably, the reduction peaks of $CuO/Nd_2Ce_2O_7$ and $CuO/Sm_2Ce_2O_7$ associated with the higher-temperature region were less pronounced than those of the other catalysts.

After subtracting the H_2 consumption of the corresponding bare supports, the H/Cu atomic ratios were calculated and are summarized in Supplementary Table 3[21]. The ratios were close to the theoretical stoichiometric value for the reduction of Cu^{2+} to metallic Cu^0, suggesting that most copper species were reduced under the applied conditions. Deviations from the theoretical value may indicate that a fraction of the copper species remained partially reduced. These results provide further insight into the reduction behavior of the supported copper species.

The reduction peak temperatures also varied with the rare-earth cation in the support. $CuO/La_2Ce_2O_7$ exhibited the highest reduction temperature (252 °C), followed by $CuO/Y_2Ce_2O_7$ (217 °C), $CuO/Nd_2Ce_2O_7$ (207 °C), and $CuO/Sm_2Ce_2O_7$ (197 °C). The relatively high reduction temperatures of $CuO/La_2Ce_2O_7$ and $CuO/Y_2Ce_2O_7$ may indicate stronger interactions between the copper species and the supports. Such interactions may influence copper reducibility and the evolution of active copper species under reaction conditions.

Surface basicity is another property that may influence MSR performance by affecting reactant adsorption and activation[41]. CO_2-TPD was therefore used to characterize the surface basic sites of the catalysts. As

shown in Figure 9B, the CO_2 desorption profiles contained features below and above 400 °C, which were assigned to weak and strong basic sites, respectively. Because MSR was performed below 400 °C in this study, weak basic sites may be particularly relevant to reactant adsorption under the investigated conditions. The quantitative results in Supplementary Table 3 show that $CuO/La_2Ce_2O_7$ possessed the largest number of weak basic sites among the four catalysts.

Figure 9C compares the CH_3OH conversion with the number of weak basic sites. $CuO/La_2Ce_2O_7$ exhibited both the highest CH_3OH conversion and the largest population of weak basic sites. However, $CuO/Y_2Ce_2O_7$ also showed high CH_3OH conversion despite having substantially fewer weak basic sites. This comparison indicates that weak basic sites alone cannot account for the differences in catalytic activity. Instead, their contribution should be considered together with other catalyst properties, including copper dispersion, surface oxygen species, oxygen-exchange behavior, and the Cu^+/Cu^0 balance.

Surface species and possible reaction pathway probed by *in situ* DRIFTS

The *in situ* DRIFTS experiments were conducted on the four catalysts under the same MSR conditions as those used in steady-state reaction tests. The catalysts were pre-reduced at 300 °C in an H_2/Ar flow for 40 min. After purging with Ar for 40 min, a methanol and steam gas mixture with a CH_3OH/H_2O molar ratio of 1:1.5 was introduced, and the infrared signals were collected at 300 °C.

Specifically, the bands at 3,700 and 3,100 cm^{-1} correspond to the stretching vibrations of the O-H bonds. The bands at 2,830 and 1,057 cm^{-1} are attributable to C-H and C-O stretching of adsorbed methoxy (OCH_3), respectively. The features between 1,370 and 1,600 cm^{-1} correspond to the asymmetric and symmetric O-C-O stretching modes of formate, with the peaks at 1,585 and 1,330 cm^{-1} assigned to monodentate (m-HCOO*) and bidentate (bi-HCOO*) formate, respectively. In addition, the band at 1,427 cm^{-1} is ascribed to carbonate (CO_3^{2-})[7,16,19,21,22,42].

As shown in Figure 10A-D, the four catalysts exhibited similar characteristic bands associated with hydroxyl, methoxy, formate, and carbonate species, indicating the presence of similar adsorbed species under the investigated MSR conditions. The evolution of the spectra indicated changes in the surface populations of methoxy and formate species during the reaction. These observations are consistent with a possible formate-mediated pathway over $CuO/Ln_2Ce_2O_7$ (Ln = La, Nd, Sm, and Y). Among the four catalysts, $CuO/La_2Ce_2O_7$ exhibited more pronounced bands associated with these surface species [Figure 10A], which may reflect differences in adsorption and surface coverage[22].

CONCLUSIONS

A series of $CuO/Ln_2Ce_2O_7$ (Ln = La, Nd, Sm, and Y) catalysts supported on defective fluorite-type oxides were prepared and evaluated for MSR. The main findings are as follows:

(1) $CuO/La_2Ce_2O_7$ exhibited the best MSR performance among the four catalysts, achieving 54% CH_3OH conversion and an H_2 production rate of 741 mmol $H_2 \cdot g_{cat.} \cdot h^{-1}$ at 360 °C, with a CO selectivity of 1.7%. It also showed the highest reaction rate and turnover frequency (329 h^{-1}), together with the lowest apparent activation energy (59 $kJ \cdot mol^{-1}$).

(2) The optimal performance of $CuO/La_2Ce_2O_7$ was associated with several physicochemical properties: a high proportion of surface-adsorbed oxygen species, a relatively high Ce^{3+} fraction, the lowest oxygen-exchange onset temperature (145 °C), and the largest population of weak basic sites. It also exhibited the highest Cu dispersion (43.6%) and smallest Cu grain size (2.4 nm). Its Cu^+/Cu^0 ratio remained nearly unchanged, decreasing from 1.02 after reduction to 1.00 after MSR.

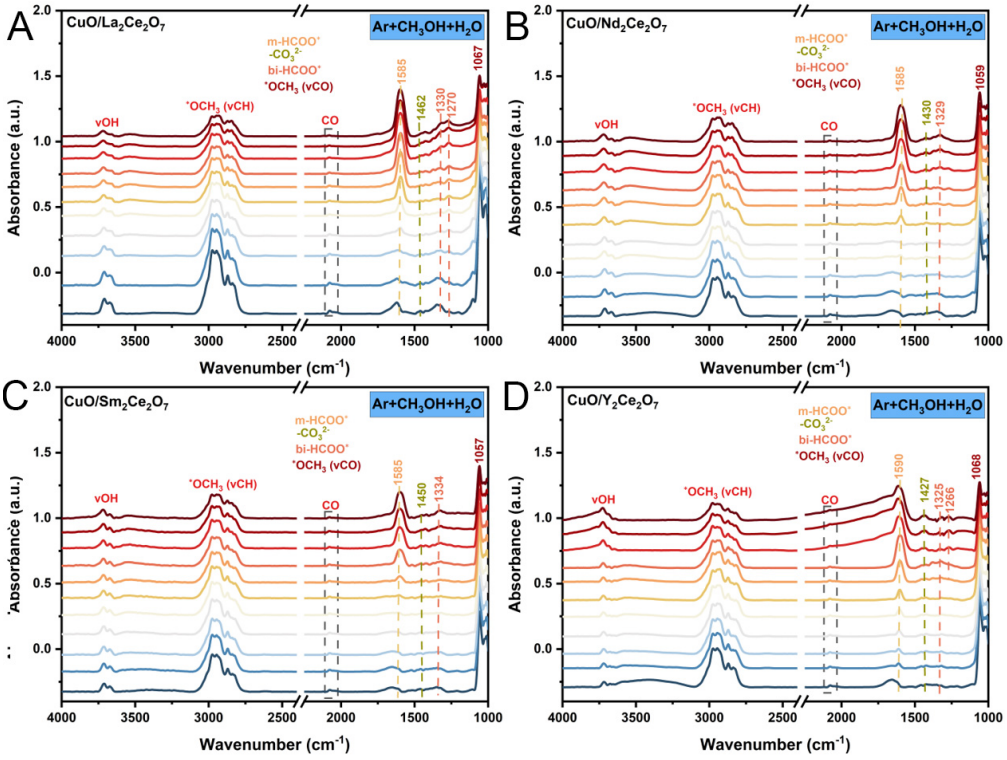

Figure 10. *In situ* DRIFTS experiments of methanol steam reforming on pre-reduced catalysts: (A) $CuO/La_2Ce_2O_7$; (B) $CuO/Nd_2Ce_2O_7$; (C) $CuO/Sm_2Ce_2O_7$; (D) $CuO/Y_2Ce_2O_7$. DRIFTS: Diffuse reflectance infrared Fourier transform spectroscopy。

(3) *In situ* DRIFTS identified adsorbed methoxy and formate species on all four catalysts, consistent with a possible formate-mediated pathway.

DECLARATIONS

Authors' contributions

Writing-original draft: Zhang, T.
Visualization: Zhang, T.; Liu, X.; Ma, J.; Wang, X.
Methodology: Zhang, T.
Investigation: Zhang, T.
Formal analysis: Zhang, T.; Liu, X.; Pang, X.; Ke, Y.; Ma, J.; Wang, X.
Data curation: Zhang, T.; Liu, X.; Pang, X.; Ke, Y.; Ma, J.
Conceptualization: Liu, X.; Ma, J.; Wang, X.
Software: Pang, X.; Xu, J.
Funding acquisition: Xu, J.; Wang, X.; Wang, X.
Resources: Xu, J.
Writing- review & editing: Wang, X.
Supervision: Wang, X.
Project administration: Wang, X.

Availability of data and materials

The data supporting the findings of this study are available within this article and its Supplementary Materials. Further data are available from the corresponding authors upon request.

AI and AI-assisted tools statement

Not applicable.

Financial support and sponsorship.

This work was financially supported by the National Natural Science Foundation of China (22572082, 22462011, 22566022, 22262021), the Natural Science Foundation of Jiangxi Province (20242BAB26029, 20232ACB213002, 20252BAC240720), the Interdisciplinary Innovation Fund of Natural Science, Nanchang University (XX202505300004), and the Key Laboratory Foundation of Jiangxi Province for Environment and Energy Catalysis (20242BCC32041).

Conflicts of interest

All authors declare that there are no conflicts of interest.

Ethical approval and consent to participate

Not applicable.

Consent for publication

Not applicable.

Copyright

© The Author(s) 2026.

Supplementary Materials

Supplementary Materials

REFERENCES

1. Zong, K.; Guan, B.; Zhu, L.; et al. Research progress on methanol steam reforming for hydrogen production: from catalyst design to reactor engineering. *Fuel* **2027**, *427*, 139653. DOI
2. Ishaq, H.; Dincer, I.; Crawford, C. A review on hydrogen production and utilization: Challenges and opportunities. *Int. J. Hydrogen. Energy.* **2022**, *47*, 26238-64. DOI
3. Hassan, A. Controversial mechanisms of methanol steam reforming: a review. *Int. J. Hydrogen. Energy.* **2024**, *93*, 1487-501. DOI
4. Gordon, J. A.; Balta-ozkan, N.; Nabavi, S. A. Hopes and fears for a sustainable energy future: Enter the hydrogen acceptance matrix. *Int. J. Hydrogen. Energy.* **2024**, *60*, 1170-91. DOI
5. Agyekum, E. B.; Nutakor, C.; Khan, T.; Adegboye, O. R.; Odoi-Yorke, F.; Okonkwo, P. C. Analyzing the research trends in the direction of hydrogen storage - a look into the past, present and future for the various technologies. *Int. J. Hydrogen. Energy.* **2024**, *74*, 259-75. DOI
6. Tang, X.; Li, J.; Fang, Z.; et al. Single Ni-inserted Cu (1 1 1) surface: a DFT study of adsorption and reaction mechanisms of methanol steam reforming. *Appl. Surf. Sci.* **2022**, *596*, 153635. DOI
7. Jin, Q.; Chen, S.; Meng, X.; et al. Methanol steam reforming for hydrogen production over Ni/ZrO_2 catalyst: comparison of thermal and non-thermal plasma catalysis. *Catal. Today.* **2024**, *425*, 114360. DOI
8. Reyna-Alvarado, J.; López-Galán, O. A.; Ramos, M.; Rodríguez, J.; Pérez-Hernández, R. A theoretical catalytic mechanism for methanol reforming in CeO_2 vs Ni/CeO_2 by energy transition states profiles. *Catal. Today.* **2022**, *392-393*, 146-53. DOI
9. Hu, B.; Shu, R.; Tian, Z.; Wang, C.; Chen, Y.; Xu, Y. Enhancement of hydrogen production *via* methanol steam reforming using a Ni-based catalyst supported by spongy mesoporous alumina. *Green. Chem.* **2024**, *26*, 5485-98. DOI
10. Lu, J.; Xu, M.; Yang, M.; et al. Methanol steam reforming for hydrogen production over NiO/NaOH catalyst: Relationship between crystal facet and sodium ions. *Int. J. Hydrogen. Energy.* **2025**, *101*, 403-18. DOI
11. Lian, H.; Geng, S.; Wang, Y.; et al. Plasma-enhanced methanol steam reforming over Pt/In_2O_3-ZnO/Al_2O_3 catalyst with ultralow Pt-loading for in-situ H_2 production. *Chem. Eng. J.* **2025**, *503*, 158479. DOI
12. Wang, X.; Li, D.; Gao, Z.; Guo, Y.; Zhang, H.; Ma, D. The nature of interfacial catalysis over Pt/$NiAl_2O_4$ for hydrogen production from methanol reforming reaction. *J. Am. Chem. Soc.* **2023**, *145*, 905-18. DOI
13. Pang, S.; Dou, X.; Zhao, W.; et al. A review on the design strategies of copper-based catalysts for enhanced activity and stability in methanol reforming to hydrogen. *Nanomaterials. (Basel).* **2025**, *15*, 1118. DOI PubMed PMC
14. Chen, X.; Li, X.; Yang, Q.; Li, C. Methanol steam reforming for hydrogen production over CuZnZrO_x: promotion effect of Cu. *ACS. Appl. Energy. Mater.* **2023**, *6*, 10061-9. DOI
15. Sun, Z.; Yu, S.; Toan, S.; Abiev, R.; Fan, M.; Sun, Z. Enabling low-temperature methanol activation via lattice oxygen induced Cu-O-Cr catalysis. *ACS. Catal.* **2023**, *13*, 13704-16. DOI

16. Meng, H.; Shen, T.; Yin, Z.; et al. Embedded-type Cu nanoparticle with largely enhanced catalytic activity and stability toward methanol steam reforming. *Angew. Chem. Int. Ed. Engl.* **2025**, *64*, e202506458. DOI
17. Mao, Q.; Gao, Z.; Liu, X.; Guo, Y.; Wang, Y.; Ma, D. The Cu-Al_2O_3 interface: an unignorable active site for methanol steam reforming hydrogen production. *Catal. Sci. Technol.* **2024**, *14*, 3448-58. DOI
18. Tuo, Y.; Zhao, H.; Chen, X.; et al. Advances in Cu-based catalysts for methanol steam reforming: mechanistic insights and atomic-level design. *J. Energy. Chem.* **2026**, *112*, 64-89. DOI
19. Li, D.; Xu, F.; Tang, X.; et al. Induced activation of the commercial Cu/ZnO/Al_2O_3 catalyst for the steam reforming of methanol. *Nat. Catal.* **2022**, *5*, 99-108. DOI
20. Xu, X.; Lan, T.; Zhao, G.; Nie, Q.; Jiang, F.; Lu, Y. Interface-hydroxyl enabling methanol steam reforming toward CO-free hydrogen production over inverse ZrO_2/Cu catalyst. *Appl. Catal. B. Environ.* **2023**, *334*, 122839. DOI
21. Jiang, L.; Yuan, S.; Ma, J.; et al. Enhancing the reactivity of Cu/Al_2O_3 for methanol steam reforming through adding CrO_x: unraveling reaction pathways and the mechanism for improvement. *ACS. Catal.* **2025**, *15*, 7138-52. DOI
22. Meng, H.; Yang, Y.; Shen, T.; et al. Designing Cu^0-Cu^+ dual sites for improved C-H bond fracture towards methanol steam reforming. *Nat. Commun.* **2023**, *14*, 7980. DOI PubMed PMC
23. Jiang, W.; Liu, A.; Yao, M.; Zhang, Y.; Fu, P. Achieving efficient almost CO-free hydrogen production from methanol steam reforming on Cu modified α-MoC. *RSC. Adv.* **2024**, *14*, 2036-47. DOI PubMed PMC
24. Yin, X.; Tang, L.; Zhan, Z.; et al. Highly efficient hydrogen production via photothermal-catalytic methanol steam reforming over high-entropy metal oxides. *Sci. Bull. (Beijing).* **2026**, *71*, 2542-51. DOI
25. Montini, T.; Melchionna, M.; Monai, M.; Fornasiero, P. Fundamentals and catalytic applications of CeO_2-based materials. *Chem. Rev.* **2016**, *116*, 5987-6041. DOI PubMed
26. Ahn, S.; Jang, W.; Shim, J.; Jeon, B.; Roh, H. CeO_2-based oxygen storage capacity materials in environmental and energy catalysis for carbon neutrality: extended application and key catalytic properties. *Catal. Rev.* **2024**, *66*, 1316-99. DOI
27. Vilela, V. B.; Thyssen, V. V.; Rodrigues, L. N.; Fonsca, C. Enhancing the catalytic activity of lanthanum-ceria fluorite for methane conversion in SOFC. *Meet. Abstr.* **2021**, *MA2021-03*, 246-246. DOI
28. Singh, Pal. R.; Rana, S.; Kumar, Sharma. S.; et al. Enhancement of oxygen vacancy sites of $La_{2-x}M_xCe_2O_{7-\delta}$ (M = Ca, Ba, Sr) catalyst for the low temperature oxidative coupling of Methane: a combined DFT and experimental study. *Chem. Eng. J.* **2023**, *458*, 141379. DOI
29. Mukherjee, D.; Rao, B. G.; Reddy, B. M. Characterization of ceria-based nano-oxide catalysts by Raman spectroscopy. *Top. Catal.* **2017**, *60*, 1673-81. DOI
30. Wang, C.; Huang, W.; Wang, Y.; et al. Synthesis of monodispersed $La_2Ce_2O_7$ nanocrystals via hydrothermal method: A study of crystal growth and sintering behavior. *Int. J. Refract. Met. H.* **2012**, *31*, 242-6. DOI
31. Xu, Y.; Wang, F.; Liu, X.; et al. Resolving a decade-long question of oxygen defects in raman spectra of ceria-based catalysts at atomic level. *J. Phys. Chem. C.* **2019**, *123*, 18889-94. DOI
32. Bhaskaran, A.; Kothoori, N. P. S.; Samanta, P. K.; et al. $La_{2-x}Sr_xCe_{2-y}Ni_yO_7$ catalysts with interstitial nickel for enhanced dry reforming of methane. *ACS. Appl. Mater. Interfaces.* **2025**, *17*, 61941-54. DOI PubMed PMC
33. Ning, H.; Li, L.; Ding, C.; et al. Oxygen vacancy engineering in template-synthesized cu Ce catalysts for enhanced low-temperature preferential CO oxidation. *Sep. Purif. Technol.* **2026**, *390*, 136982. DOI
34. Wu, T.; Zhang, P.; Wei, Y.; et al. Surface oxygen vacancies induced by calcium substitution in macroporous $La_2Ce_{2-x}Ca_xO_{7-\delta}$ catalysts for boosting low-temperature oxidative coupling of methane. *ACS. Catal.* **2024**, *14*, 1882-902. DOI
35. Cheng, Z.; Li, Y.; Wang, M.; et al. Construction of porous Cu/CeO_2 catalyst with abundant interfacial sites for effective methanol steam reforming. *J. Colloid. Interface. Sci.* **2025**, *677*, 55-67. DOI
36. Li, D.; Qiu, R.; Moskowitz, B. M.; et al. Nature of the active sites and reaction mechanism during methanol steam reforming over Cu/ZnO: an isotopic modulated excitation diffuse reflectance infrared Fourier transform spectroscopy study. *J. Am. Chem. Soc.* **2025**, *147*, 24040-9. DOI
37. Köwitsch, N.; Thoni, L.; Klemmed, B.; et al. Proving a paradigm in methanol steam reforming: catalytically highly selective In_xPd_y/In_2O_3 interfaces. *ACS. Catal.* **2021**, *11*, 304-12. DOI
38. Liu, D.; Zhang, M.; Zhao, L.; Guo, X.; Xu, G.; He, H. Mechanistic insights into methanol steam reforming on copper catalysts: dynamics of active sites and reaction pathway. *J. Catal.* **2025**, *442*, 115922. DOI
39. Ma, F.; Zhang, P.; Zheng, X.; et al. Steering the site distance of atomic Cu-Cu pairs by first-shell halogen coordination boosts CO_2-to-C_2 selectivity. *Angew. Chem. Int. Ed. Engl.* **2024**, *63*, e202412785. DOI
40. Liu, X.; Wang, K.; Ran, Q.; et al. Synergetic Cu^0 and Cu^+ on the surface of Al_2O_3 support enhancing methanol steam reforming reaction. *Surf. Interfaces.* **2024**, *51*, 104633. DOI

41. Xu, X.; Shuai, K.; Xu, B. Review on copper and palladium based catalysts for methanol steam reforming to produce hydrogen. *Catalysts* **2017**, *7*, 183. DOI

42. Hadi, M.; Alavi, S. M.; Rezaei, M.; Akbari, E.; Tabarkhoon, F. Methanol steam reforming over $CuO/MgAl_2O_4$ nanocatalysts: influence of copper oxide loading and process parameters on hydrogen production. *Fuel* **2025**, *399*, 135678. DOI

Disclaimer/Publisher's Note: All statements, opinions, and data contained in this publication are solely those of the individual author(s) and contributor(s) and do not necessarily reflect those of OAE and/or the editor(s). OAE and/or the editor(s) disclaim any responsibility for harm to persons or property resulting from the use of any ideas, methods, instructions, or products mentioned in the content.

© The Author(s) 2026. Open Access This article is licensed under a Creative Commons Attribution 4.0 International License (https://creativecommons.org/licenses/by/4.0/), which permits unrestricted use, sharing, adaptation, distribution and reproduction in any medium or format, for any purpose, even commercially, as long as you give appropriate credit to the original author(s) and the source, provide a link to the Creative Commons license, and indicate if changes were made.